Article

Ice front blocking of ocean heat transport to an Antarctic ice shelf

A. K. Wåhlin[1✉], N. Steiger[2,3], E. Darelius[2,3], K. M. Assmann[1,12], M. S. Glessmer[4], H. K. Ha[5], L. Herraiz-Borreguero[6,7], C. Heuzé[8], A. Jenkins[9,13], T. W. Kim[10], A. K. Mazur[1], J. Sommeria[11] & S. Viboud[11]

Mass loss from the Antarctic Ice Sheet to the ocean has increased in recent decades, largely because the thinning of its floating ice shelves has allowed the outflow of grounded ice to accelerate[1,2]. Enhanced basal melting of the ice shelves is thought to be the ultimate driver of change[2,3], motivating a recent focus on the processes that control ocean heat transport onto and across the seabed of the Antarctic continental shelf towards the ice[4–6]. However, the shoreward heat flux typically far exceeds that required to match observed melt rates[2,7,8], suggesting that other critical controls exist. Here we show that the depth-independent (barotropic) component of the heat flow towards an ice shelf is blocked by the marked step shape of the ice front, and that only the depth-varying (baroclinic) component, which is typically much smaller, can enter the sub-ice cavity. Our results arise from direct observations of the Getz Ice Shelf system and laboratory experiments on a rotating platform. A similar blocking of the barotropic component may occur in other areas with comparable ice–bathymetry configurations, which may explain why changes in the density structure of the water column have been found to be a better indicator of basal melt rate variability than the heat transported onto the continental shelf[9]. Representing the step topography of the ice front accurately in models is thus important for simulating ocean heat fluxes and induced melt rates.

The fate of the Antarctic Ice Sheet is the greatest remaining uncertainty when predicting future sea level[10]. Estimates of its contribution to global sea-level rise range[10–12] from none to a catastrophic >5 cm yr⁻¹ (4 m by the year 2100). The ice sheet drains into the ocean, where it terminates in floating ice shelves, overlying vast sub-ice cavities. These buttress the flow of the ice sheet, regulating the speed at which it flows into the ocean[13]. Rapid thinning of ice shelves in coastal regions with warm ocean water on the continental shelf is accelerating the outflow from the ice sheet[1,2]. The perceived reason—although rarely observed directly[14]—is that ocean currents deliver more warm water to the ice shelf cavities, causing increased basal melt. These currents originate in a reservoir of warm and salty water, known as Circumpolar Deep Water (CDW)[15], residing at 300–1,000 m depth in the Southern Ocean. Substantial amounts of dense CDW are carried onto the continental shelf by various mechanisms[4–7,16], but only a fraction of this is needed to explain observed basal melt rates[17].

The CDW flows southwards in deep troughs that crosscut the continental shelf[4,18–21]. The currents are steered by the bathymetry and move with shallower water to the left of the flow direction[22–24], so southward transport occurs along the eastern, and northward on the western, flanks of the troughs[19,25]. The flow is a combination of barotropic (vertically constant, wind-driven[26,27]) and baroclinic (vertically varying, density-driven) currents. Although the barotropic velocities often dominate[27,28], most of the heat is contained in the warm dense water below the thermocline, where the baroclinic component typically enhances the flow.

In order to enter the ice shelf cavity, the currents must pass the ice front—a wall of ice protruding from the surface to depths of 250–500 m. This front imposes an abrupt change in the thickness of the water column, potentially disrupting the topographically steered flow towards it[29]. Logistical challenges generally prevent observations near the ice front, and estimates of oceanic heat transport towards the ice shelves are based on moorings placed at a 'safe' distance (at least a few kilometres) away from the ice front.

To examine the effect of the ice front on the along-trough current, we placed three moorings—equipped with velocity profilers and loggers for temperature, salinity and pressure —in a deep trough leading to Getz Ice Shelf (Fig. 1). Two of the moorings (GW1, GW2) were positioned 14 km and 11 km away from the ice front at depths of 600 m and 700 m, respectively, while the third (GW3) was placed 700–800 m from the front at 600 m depth. The ice front draught is[30] 250–300 m, and its position was constant during the two years of measurements (Fig. 1).

[1]Department of Marine Sciences, University of Gothenburg, Gothenburg, Sweden. [2]Bjerknes Centre for Climate Research, University of Bergen, Bergen, Norway. [3]Geophysical Institute, University of Bergen, Bergen, Norway. [4]Leibniz Institute for Science and Mathematics Education, Kiel, Germany. [5]Department of Ocean Sciences, Inha University, Incheon, South Korea. [6]Commonwealth Scientific and Industrial Research Organisation (CSIRO), Hobart, Tasmania, Australia. [7]Centre for Southern Hemisphere Oceans Research, Hobart, Tasmania, Australia. [8]Department of Earth Sciences, University of Gothenburg, Gothenburg, Sweden. [9]British Antarctic Survey, Cambridge, UK. [10]Korea Polar Research Institute, Incheon, South Korea. [11]Laboratoire des Écoulements Géophysiques et Industriels, L'université Grenoble-Alpes, Grenoble, France. [12]Present address: Institute of Marine Research, Tromsø, Norway. [13]Present address: Department of Geography and Environmental Sciences, Northumbria University, Newcastle upon Tyne, UK. ✉e-mail: awahlin@gu.se
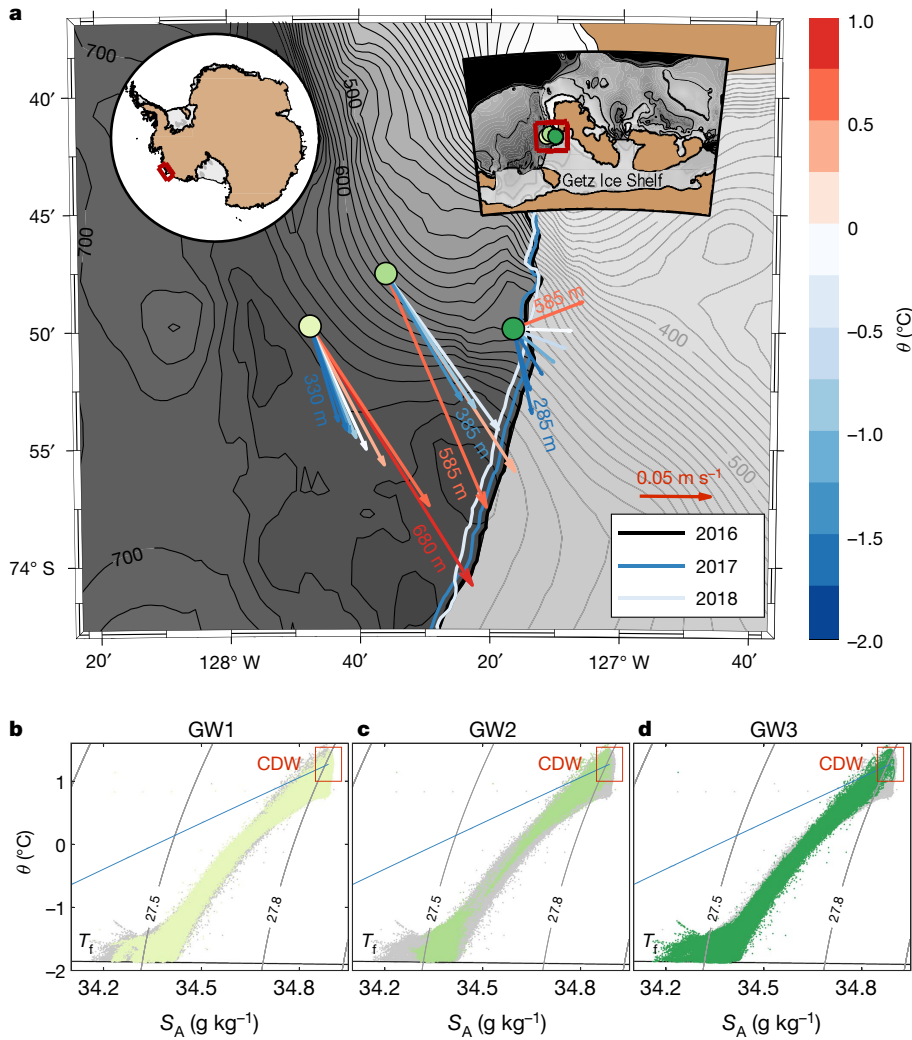
Fig. 1 | Blocking of topographically steered current at the Getz Ice Shelf front. a, Main panel, mooring locations and time-averaged velocities from three moorings (GW1, very pale green; GW2, light green; GW3, dark green) are shown as feather plots on top of the local bathymetry[31]. Velocities are colour-coded with conservative temperature θ and depth-averaged in 50-m bins starting at the bottom. The lowermost (red, warmest) and uppermost (blue, coldest) bin depths are quoted near the corresponding arrows. Also shown is the location of the ice front in January 2016, January 2017 and January 2018 (black, dark blue and pale blue lines, respectively; see Methods). The two insets show the study area in Antarctica (left) and the Getz Ice Shelf (right). **b**–**d**, Conservative temperature θ versus absolute salinity S_A for GW1 (**b**), GW2 (**c**) and GW3 (**d**) in green hues; grey dots are the data from all moorings. Red squares indicate Circumpolar Deep Water temperature range and salinity range[15], the blue thick line is the mixing line between CDW and glacier meltwater[35] and the lower black thin line is the freezing point (T_f). The lack of data points near salinity 34.5 g kg^{-1} in GW2 is due to the fact that GW2 had only two salinity sensors (Extended Data Fig. 2), of which one was faulty for a period of time (see Methods). Mooring temperature and velocity time series are shown in Extended Data Figs. 1–3.

Feather plots of the average velocity at various depths for the three moorings (Fig. 1, Methods; full time series in Extended Data Figs. 1–3) show a persistent current of up to 30 cm s^{-1} directed towards the ice shelf, parallel to the local bathymetry[8]. The velocity at the near-front mooring was less than one-third of those in the channel and deflected westwards by up to 45°. Separating the currents into barotropic and baroclinic components (Fig. 2, Methods, Extended Data Figs. 4, 5) reveals that while GW1 and GW2 had substantial barotropic along-slope flow (7.5 cm s^{-1} and 10 cm s^{-1}, respectively) with a baroclinic amplification in the warm bottom layer, the velocity at GW3 had a comparatively small barotropic component (0.1 cm s^{-1}) and was dominated by the baroclinic flow in the warm bottom layer. The direction of the baroclinic flow at GW3 is into the ice shelf cavity, that is, parallel to the local topography and orthogonal to the ice front. It should be noted, however, that the bathymetry underneath the ice shelf has not yet been surveyed[31]. In the un-surveyed areas south of mooring GW3, the compilation used in Fig. 1 is based on gravity inversions associated with high uncertainty[31]. If there are underwater features such as submarine ridges and seamounts present underneath the ice shelf, these might redirect the flow.

The strong correlation between the velocity at GW3 and the baroclinic velocities at GW1 and GW2 (Fig. 2, Table 1 entries in italic font) indicates that the baroclinic current component at GW1 and GW2 is continuing to GW3. The barotropic component, however, had only weak correlation to the GW3 velocity, suggesting that it is diverted along the ice shelf front before it reaches GW3 (Figs. 1, 2). This is further evidenced by the high correlation between bottom temperature/density anomalies at

GW2 and GW3 (both at the 600 m isobaths; Table 1, italic font). The barotropic component of the flow carries about 70% of the total heat transport (Extended Data Table 1, Extended Data Fig. 6, Methods) at GW1 and GW2, similar to values on the central Amundsen Shelf[27], while at GW3 it carries only 3%–10% (according to the more realistic methods (ii) or (iii) for estimating barotropic velocity; see Methods). The heat transport is dominated by the mean flow rather than the fluctuations assessed in Table 1 (Extended Data Table 1).

The observed behaviour of the velocity components at the ice front can be explained by geostrophic ocean dynamics[22,29]. Geostrophic currents are non-divergent and therefore flow parallel to lines of constant water column thickness, or, in the open ocean, lines of constant depth[22,24]. This is the reason why the currents in the deep troughs are so strongly steered by the (comparatively gentle) topography. However, where a floating ice shelf with a considerable draught overlies the ocean, the water column thickness is no longer equal to the depth. Applied to the present setting, this means that barotropic currents approaching the ice front along depth contours will be diverted owing to the change in water column thickness (Methods) and may be blocked entirely without reaching the ice shelf cavity[29]. Baroclinic flow, on the other hand, can move along depth contours into the ice shelf cavity, provided the thermocline is deeper than the ice shelf draught.

In order to explore this phenomenon in a controlled environment, experiments were conducted on the 13-m-diameter rotating Coriolis platform in Grenoble, France. A simplified bathymetry—a V-shaped trough—was placed in a 90-cm-deep tank filled with fresh water (Fig. 3, Extended Data Figs. 7, 8). A source was placed on the right flank (facing
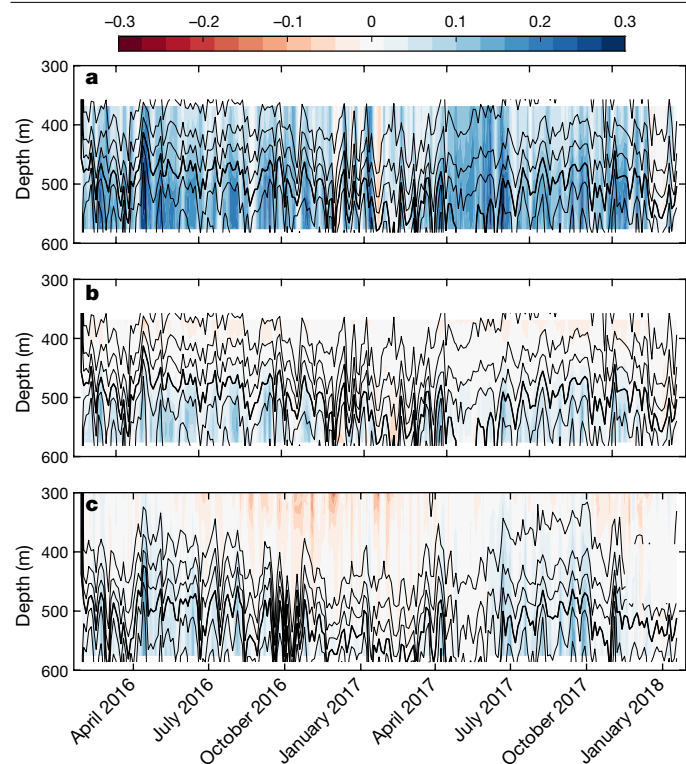
Fig. 2 | The baroclinic velocity component at GW2 is similar to the total velocity at GW3. Three-day-average along-slope velocity (colour bar; m s⁻¹) with isotherms (black contours, every 0.5 °C; the thick black line shows the 0 °C isotherm). **a**, Total along-slope velocity at GW2. **b**, Baroclinic velocity component (Methods) at GW2. **c**, Total along-slope velocity at GW3. Note that the topmost sensor on GW2 was at 357 m depth, while at GW3 it was at 288 m depth (Extended Data Figs. 2, 3).

Fig. 3 | Experimental set-up and difference between barotropic and baroclinic flow. a, Sketch of the experiment, indicating the location of the cross-sections shown below and the flow path outside (red arrow) and underneath (pale red arrow) the ice shelf. **b**–**d**, Side-view sketches of the ice shelf (light blue), bottom (grey) and water (dark blue) with ice shelf draught 0 cm (**b**), tilted (**c**) and 30 cm (**d**). **e**, **f**, Photographs from underneath the ice shelf, facing north, showing southward flow (indicated by black circled dot). In **e** the flow is barotropic and the boundary between the southward-moving water (light grey) and the northward-moving water (dark) is nearly vertical. In **f** the flow is baroclinic and the dense water is yellow with a sloping surface.
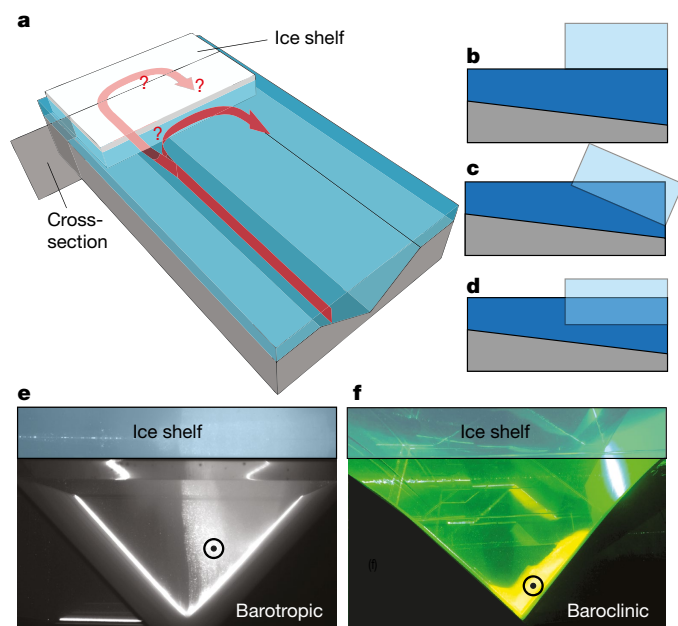
north) of the trough, pumping fresh water to set up a barotropic current, or saline (denser) water for a baroclinic bottom current. At the far end of the trough, a plexiglass ice shelf with adjustable draught was placed. A detailed description of the experimental set-up is presented in Methods.

The experimental results agree qualitatively with the geostrophic dynamics outlined above. The current followed the trough flank towards the ice shelf, and away from it on the opposite side, similarly to observations[19,25] (Fig. 4). Placing an ice shelf with near-zero draught on top of the trough (Fig. 4a) had no visible impact on the circulation. However, a sloping ice shelf with zero draught at the front and 30 cm at the back (Fig. 4b) caused the barotropic flow to change direction and follow lines

Table 1 | Correlation between Getz moorings GW1–3

	ρ_B at GW1	T_B at GW2	ρ_B at GW3	U at GW3
T_B at GW2	**0.62 (0.55)**	NA	ND	ND
ρ_B at GW3	**0.67 (0.58)**	**0.92 (0.83)**	NA	ND
U_{BC} at GW1	**0.54 (0.46)**	**0.71 (0.62)**	**0.77 (0.67)**	**0.66 (0.53)**
U_{BT} at GW1	−0.09 (−0.03)	−0.08 (0.05)	−0.25 (−0.1)	-0.08 (0.02)
U_{BC} at GW2	**0.43 (0.36)**	**0.54 (0.49)**	**0.53 (0.45)**	**0.67 (0.51)**
U_{BT} at GW2	0.15 (0.03)	0.20 (0.01)	0.09 (0.1)	0.23 (0.23)
U at GW3	**0.51 (0.36)**	**0.5 (0.39)**	**0.65 (0.57)**	NA

Correlation coefficients between combinations of bottom density ρ_B (or bottom temperature T_B for GW2, which had a broken conductivity sensor and hence no bottom density) and along-slope bottom velocity U, as well as the barotropic (U_{BT}) and baroclinic (U_{BC}) components of bottom velocity for the three moorings, GW1, GW2 and GW3. Numbers shown are correlations between the indicated quantities based on 10-day averages and, within parentheses, three-day averages. Bold numbers indicate that the correlations are significant at the 99.99% level. Italic font indicates the key correlations discussed in the text. NA, not applicable; ND, not determined.

of constant water thickness into the ice shelf cavity. A horizontal ice shelf with 30 cm draught (Fig. 4c) blocked the current from entering the cavity. The baroclinic currents (Extended Data Fig. 9) continued mostly unaffected into the ice shelf cavity for all ice shelf draughts and shapes.

The observational and experimental results presented here enhance our understanding of how changes in oceanic heat transport on the continental shelf can affect basal melt. Barotropic flow is blocked, either partially or entirely, depending on the ice front geometry, from entering the cavity. Changes in the water temperature and/or baroclinic flow, on the other hand, will change the amount of heat that flows into the cavity. How much of it is ultimately used for basal melting depends on the cavity efficiency[32]. The results explain why changes in the thickness of the warm water layer seem to be a more reliable indicator of melt rate variability than, for example, ocean transports across the shelf break. Changes in the vertical structure of the water column is a better diagnostic of the critical baroclinic heat transport.

Because flows towards ice shelf cavities nearly always have a substantial barotropic component[8,26,27,33], the findings have broad implications for calculations of ocean heat transport to ice shelf cavities. For example, the measured heat transport along the Siple Trough is 2.27–2.8 TW (Extended Data Table 1)—sufficient to melt about 250–300 Gt ice per year and twice the total basal melt (136 Gt yr⁻¹) that the entire Getz Ice Shelf experiences[17]. However, owing to the abrupt front shape, only one-sixth (0.47 TW) of the heat that flows past GW1 and GW2 enters the cavity. The results indicate that the floating ice shelves not only give back-stress, mechanically slowing down the inland ice sheet[13], but also protect the vulnerable grounded ice by blocking a large portion of the warm ocean currents from reaching the cavity. The thickness and shape of the ice front may provide a critical and evolving control that needs to be incorporated accurately in models: were an ice front
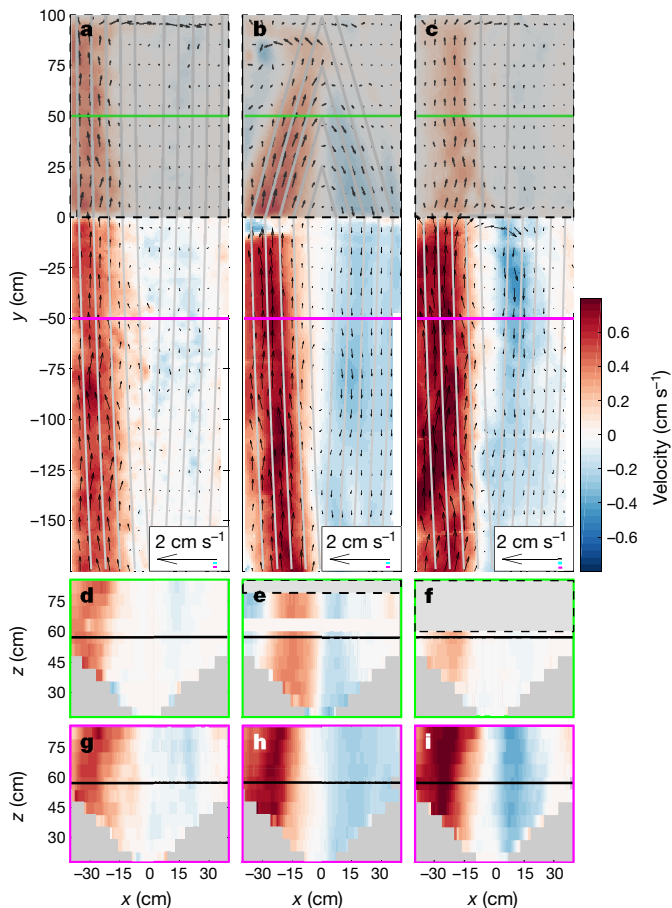
Fig. 4 | Blocking of depth-independent currents in laboratory. Horizontal velocities from the laboratory experiments are presented for barotropic flow with the three different ice shelf configurations shown in Fig. 3b–d. Colours indicate velocity in the *y* direction, arrows indicate velocity vectors. **a**–**c**, Velocities at the horizontal plane in the centre of the current (black lines in **d**–**i**). **d**–**f**, Velocities at vertical sections underneath the ice shelf (green lines in **a**–**c**). **g**–**i**, Velocities at vertical sections in front of the ice shelf (magenta lines in **a**–**c**). Dashed rectangles with grey shading indicate the ice shelf, grey shading in V formation indicates topography, and grey lines are lines of constant water thickness that the current is expected to follow. The cyan bar beneath the scale arrow in **a**–**c** indicate the temporal standard deviation of the velocity, and the magenta bar indicates the error (Methods).

to thin substantially, or to retreat (or advance) to a region with larger underwater features steering the warm currents towards the cavity, then the heat flux to the ice sheet could change markedly. Observations from inside the cavity[14,34] are at present rare, and more are needed to determine, for example, how much of the heat transport eventually reaches the vulnerable grounding zones.

Online content

Any methods, additional references, Nature Research reporting summaries, source data, extended data, supplementary information, acknowledgements, peer review information; details of author contributions and competing interests; and statements of data and code availability are available at https://doi.org/10.1038/s41586-020-2014-5.

1. Shepherd, A., Fricker, H. A. & Farrell, S. L. Trends and connections across the Antarctic cryosphere. *Nature* **558**, 223–232 (2018).
2. Pritchard, H. D. et al. Antarctic ice-sheet loss driven by basal melting of ice shelves. *Nature* **484**, 502–505 (2012).
3. Liu, Y. et al. Ocean-driven thinning enhances iceberg calving and retreat of Antarctic ice shelves. *Proc. Natl Acad. Sci. USA* **112**, 3263–3268 (2015).
4. Thoma, M., Jenkins, A., Holland, D. & Jacobs, S. Modelling Circumpolar Deep Water intrusions on the Amundsen Sea continental shelf, Antarctica. *Geophys. Res. Lett.* **35**, L18602 (2008).
5. Wåhlin, A. K. et al. Some implications of Ekman layer dynamics for cross-shelf exchange in the Amundsen Sea. *J. Phys. Oceanogr.* **42**, 1461–1474 (2012).
6. Darelius, E., Fer, I. & Nicholls, K. W. Observed vulnerability of Filchner-Ronne Ice Shelf to wind-driven inflow of warm deep water. *Nat. Commun.* **7**, 12300 (2016).
7. Palóczy, A., Gille, S. T. & McClean, J. L. Oceanic heat delivery to the Antarctic continental shelf: large-scale, low-frequency variability. *J. Geophys. Res.* **123**, 7678–7701 (2018).
8. Assmann, K. M., Darelius, E., Wåhlin, A. K., Kim, T. W. & Lee, S. H. Warm Circumpolar Deep Water at the western Getz Ice Shelf front, Antarctica. *Geophys. Res. Lett.* **46**, 870–878 (2019).
9. Jenkins, A. et al. West Antarctic Ice Sheet retreat in the Amundsen Sea driven by decadal oceanic variability. *Nat. Geosci.* **11**, 733–738 (2018).
10. IPCC. *Climate Change 2014: Synthesis Report. Contribution of Working Groups I, II and III to the Fifth Assessment Report of the Intergovernmental Panel on Climate Change* (eds Pachauri R. K. & Meyer L. A.) (IPCC, 2014).
11. IMBIE Team. Mass balance of the Antarctic ice sheet from 1992 to 2017. *Nature* **558**, 219–222 (2018).
12. DeConto, R. M. & Pollard, D. Contribution of Antarctica to past and future sea-level rise. *Nature* **531**, 591–597 (2016).
13. Scambos, T. A., Bohlander, J. A., Shuman, C. A. & Skvarca, P. Glacier acceleration and thinning after ice shelf collapse in the Larsen B embayment, Antarctica. *Geophys. Res. Lett.* **31**, L18402 (2004).
14. Jenkins, A. et al. Observations beneath Pine Island Glacier in West Antarctica and implications for its retreat. *Nat. Geosci.* **3**, 468–472 (2010).
15. Callahan, J. E. The structure and circulation of Deep Water in the Antarctic. *Deep-Sea Res.* **19**, 563–575 (1972).
16. Thompson, A. F., Stewart, A. L., Spence, P. & Heywood, K. J. The Antarctic Slope Current in a changing climate. *Rev. Geophys.* **56**, 741–770 (2018).
17. Depoorter, M. A. et al. Calving fluxes and basal melt rates of Antarctic ice shelves. *Nature* **502**, 89–92 (2013); correction **502**, 580 (2013).
18. Wåhlin, A. K., Yuan, X., Björk, G. & Nohr, C. Inflow of Warm Circumpolar Deep Water in the Central Amundsen Shelf. *J. Phys. Oceanogr.* **40**, 1427–1434 (2010).
19. Herraiz-Borreguero, L. et al. Circulation of modified Circumpolar Deep Water and basal melt beneath the Amery Ice Shelf, East Antarctica. *J. Geophys. Res. Oceans* **120**, 3098–3112 (2015).
20. Nakayama, Y., Menemenlis, D., Zhang, H., Schodlok, M. & Rignot, E. Origin of Circumpolar Deep Water intruding onto the Amundsen and Bellingshausen Sea continental shelves. *Nat. Commun.* **9**, 1–9 (2014).
21. St-Laurent, P., Klinck, J. M. & Dinniman, M. S. On the role of coastal troughs in the circulation of warm Circumpolar Deep Water on Antarctic shelves. *J. Phys. Oceanogr.* **43**, 51–64 (2013).
22. Cushman-Roisin, B. & Beckers, J.-M. *Introduction to Geophysical Fluid Dynamics: Physical and Numerical Aspects* (Prentice-Hall, 2011).
23. Nof, D. The translation of isolated cold eddies on a sloping bottom. *Deep-Sea Res. A* **30**, 171–182 (1983).
24. Wåhlin, A. K. Topographic advection of dense bottom water. *J. Fluid Mech.* **510**, 95–104 (2004).
25. Ha, H. K. et al. Circulation and modification of warm deep water on the central Amundsen shelf. *J. Phys. Oceanogr.* **44**, 1493–1501 (2014).
26. Wåhlin, A. K. et al. Variability of warm deep water inflow in a submarine trough on the Amundsen Sea shelf. *J. Phys. Oceanogr.* **43**, 2054–2070 (2013).
27. Kalén, O. et al. Is the oceanic heat flux on the central Amundsen sea shelf caused by barotropic or baroclinic currents? *Deep-Sea Res. II* **123**, 7–15 (2016).
28. Rignot, E., Jacobs, S., Mouginot, J. & Scheuchl, B. Ice-shelf melting around Antarctica. *Science* **341**, 266–270 (2013).
29. Grosfeld, K., Gerdes, R. & Determann, J. Thermohaline circulation and interaction between ice shelf cavities and the adjacent open ocean. *J. Geophys. Res. Oceans* **102**, 15595–15610 (1997).
30. Jacobs, S. et al. Getz Ice Shelf melting response to changes in ocean forcing. *J. Geophys. Res. Oceans* **118**, 4152–4168 (2013).
31. Arndt, J. E. et al. The International Bathymetric Chart of the Southern Ocean (IBCSO) Version 1.0 — A new bathymetric compilation covering circum-Antarctic waters. *Geophys. Res. Lett.* **40**, 3111–3117 (2013).
32. Little, C. M., Gnanadesikan, A. & Oppenheimer, M. How ice shelf morphology controls basal melting. *J. Geophys. Res.* **114**, C12007 (2009).
33. Miles, T. et al. Glider observations of the Dotson Ice Shelf outflow. *Deep-Sea Res. II* **123**, 16–29 (2016).
34. Nicholls, K. W. et al. Measurements beneath an Antarctic ice shelf using an autonomous underwater vehicle. *Geophys. Res. Lett.* **33**, L08612 (2006).
35. Gade, H. Melting of ice in sea water: a primitive model with application to the Antarctic ice shelf and icebergs. *J. Phys. Oceanogr.* **9**, 189–198 (1979).

Article

Methods

Mooring data

Three moorings were deployed on 29 January 2016 and recovered on 18 January 2018 on the western flank of Siple Island (Fig. 1). Two of the moorings were deployed 11–14 km from the ice shelf at depths of 600 m (GW2, 73° 47.6′ S, 127° 36.0′ S) and 700 m (GW1, 73° 49.8′ S, 127° 47.6′ S). The third mooring was located 700–750 m from the ice shelf at a depth of 600 m (GW3, 73° 50.0′ S, 127° 16.6′ S), within a Rossby radius (2 km) of the ice front. The moorings were equipped with sensors for temperature, conductivity and pressure from Seabird Electronics (SBE37, SBE39 and SBE56) and Acoustic Doppler Current Profilers (ADCP, Teledyne RD Instruments, 75 and 150 kHz Sentinel). The initial accuracy of the temperature data was 0.002 °C and the resolution was 0.0001 °C. The ADCP data were quality-controlled using standard criteria for filtering out bad data and outliers[36] based on quality controls on individual beams and bins recorded by the instrument each ping (percentage of good returns below 50%, average echo intensity below 40 counts, and roll and pitch of instrument exceeding 20° filtered out). The raw data (saved at 15 min temporal resolution) had standard error 1–1.5 cm s^{-1} and were averaged to hourly means.

Hydrographic measurements extended from the bottom to 357 m and 305 m below the surface for GW2 and GW1, respectively, with downward-looking ADCPs just above the top sensor, and to 288 m below the surface at GW3, with an upward-looking ADCP just below the bottom sensor (Fig. 1). Extended Data Figs. 1–3 show the northward and eastward velocities recorded at the three locations, together with temperature. Conservative temperature and absolute salinity in Fig. 1 were calculated following TEOS-10[37].

The along-slope directions were defined as true bearings of 135° for GW1, 110° for GW2 and 70° for GW3, based on the IBCSO[31] database (Fig. 1).

Ice shelf data

The position of the ice front shown in Fig. 1 was manually digitized from Sentinel-1 synthetic aperture radar images recorded in the January of 2016, 2017 and 2018. These were level-1 ground range detected images, projected to ground range using the Earth ellipsoid model WGS84 with a pixel size of 40 × 40 m. Getz Ice Shelf is characterized by surface structures parallel to the calving front[38]. This is the most common pattern observed among west Antarctic ice shelves and gives the type of calving front studied. The mean ice equivalent thickness of Getz Ice Shelf is[3] 286 m, comparable to the average of ice shelves in the Amundsen Sea (273 m). This indicates that Getz Ice Shelf is representative for the area.

Baroclinic and barotropic velocities

According to thermal wind balance[22], the baroclinic velocity component is expected to be largest in the dense layer below the thermocline and small in the well mixed water above it. Since the present velocity data do not cover the upper water column (Extended Data Fig. 1) the barotropic (U_{BT}) and baroclinic (U_{BC}) velocity components have to be estimated on the basis of the data at hand. Three different methods were employed and compared.

(i) Assuming that the barotropic velocity component is given by the vertical average of the measured water column. While this method would give an accurate estimate in flows that have a comparatively thin baroclinic layer and/or a strong barotropic current, it will probably overestimate the barotropic current in the present data since only the bottom half of the water column is measured.

(ii) Assuming that the barotropic velocity component is given by the vertical average of the velocity from 150 m above the seabed to the upper end of the measured volume. This method will give an accurate estimate when the thermocline is closer than 150 m to the seabed but will otherwise overestimate the barotropic velocity component.

(iii) Assuming that the barotropic velocity component is given by the average velocity in the water above the thermocline. This method gives

the most accurate result, but a disadvantage is that the thermocline was not always covered by the mooring data. By choosing the thermocline level to be at −0.5 °C, barotropic velocity estimates were obtained for nearly the complete record (Extended Data Figs. 1c, 2c, 3c).

Using any of the above methods, U_{BT} and U_{BC} can be calculated by

$$U_{BC}(z, t) = U(z, t) - U_{BT}(t)$$
$$U_{BT}(t) = \frac{1}{(Z_0 - Z_1)} \int_{Z_0}^{Z_1} U(\xi, t) \mathrm{d}\xi \quad (1)$$

where $U(z,t)$ is the velocity measured at the moorings for various depths z and times t, ξ is the integration variable, and the integral limits Z_0 and Z_1 are given by one of the following[27]:
(i) Z_0 is the seabed and Z_1 is the upper end of the measured water column.
(ii) $Z_0 = 150$ m above the seabed and Z_1 is the upper end of the measured water column.
(iii) Z_0 is the −0.5 °C isotherm and Z_1 is the upper end of the measured water column.

Extended Data Fig. 4 shows time series of the three estimates (i)–(iii) of the barotropic velocities over the two years. Extended Data Fig. 5 shows the average velocity (thick lines) together with the three alternative barotropic components (thin lines, Extended Data Fig. 5a), the baroclinic component (Extended Data Fig. 5b) and the temperature (Extended Data Fig. 5c). In Fig. 2 the barotropic velocity component was defined according to (ii) above, that is, red lines in Extended Data Fig. 4 and dashed lines in Extended Data Fig. 5a. Similar results were obtained using the other two definitions of Z_0 and Z_1, which is in accordance with ref. [27].

Heat transport calculations

Assuming that the width of the flow is bounded by the sloping topography (as suggested by the laboratory experiments), the heat transport H (in J s^{-1}) towards the glacier can be estimated by

$$H = W \int_D^\eta \rho C_P U(T - T_{REF}) \mathrm{d}\xi \quad (2)$$

where W (in metres) is the width of the sloping channel side, D is the bottom elevation, η is the top of the mooring, ρ (in kg m^{-3}) is density, C_P (in J K^{-1} kg^{-1}) is the specific heat capacity, U (in m s^{-1}) is the (average) along-channel velocity, T (in kelvin) is the temperature and T_{REF} the temperature to which the water cools after interaction with glacial ice. Assuming that all the water cools to freezing temperature, equation (2) is given by:

$$H = W\rho C_P \int_D^\eta U(T - T_F) \mathrm{d}z$$

where T_F (in kelvin) is the in situ freezing temperature (which decreases with pressure and salinity). The heat flux induced by the barotropic and baroclinic velocity components is then given by $H = H_{BT} + H_{BC}$ where

$$H_{BC} = W\rho C_P \int_D^\eta U_{BC}(T - T_F) \mathrm{d}z \quad (3)$$

$$H_{BT} = W\rho C_P \int_D^\eta U_{BT}(T - T_F) \mathrm{d}z \quad (4)$$

and the barotropic (U_{BT}) and baroclinic (U_{BC}) velocity components are given by equation (1). In Extended Data Fig. 6, time series of H, H_{BT} and H_{BC} were calculated using $W = 10$ km, $C_P = 3.968$ kJ kg^{-1} K^{-1}, in situ freezing temperature[39], in situ density[39], and definition (ii) for the barotropic velocity, equation (1). The temperature and velocity data were

re-gridded to a common grid using daily averages and linear interpolation in the vertical with 8 m cell size.

Extended Data Table 1 shows the temporal average of the heat flux calculated from equations (2)–(4) and each of the three methods (i)–(iii). As discussed, the barotropic velocity is probably overestimated with method (i), which gives smaller baroclinic heat flux components for all three moorings. The results of methods (ii) and (iii) are quite consistent and show that the baroclinic heat flux is about 30% at GW1 and GW2 while it is between 90% and 97% at GW3, where the average barotropic velocity is nearly zero.

Heat transport errors

The instrument error in the ADCP is a maximum of 1.5 cm s⁻¹ and the real error is substantially lower since an average over many pings was used. This error is of the same order of magnitude as the methodological uncertainty, exemplified by the three methods (Extended Data Fig. 5). In the conversion from velocity to heat transport there is an error involved in the assumption that the data at the mooring site are representative for the entire channel (equation (2)). In the absence of continuous, high-resolution sampling across the width of the channel, which would enable an exact estimate of this error, an indication of the uncertainties involved can be obtained by the difference between the results of GW1 and GW2 (Table 1), that is, about 0.5 TW or 18%. There is also an error caused by the fact that the upper part of the water column is not included in the heat flux calculations. Since the temperature above the measured volume is near freezing temperature (Extended Data Fig. 5), however, this error is relatively small.

Another source of error is the assumption that the flow is steady. By separating velocity and temperature into mean and fluctuating components, the impact of temporal variability on the average heat transport can be estimated by

$$\overline{H} = W\rho C_P \overline{\int_D^\eta (\overline{U} + U')(\overline{T} + T' - T_F)\,\mathrm{d}\xi}$$ (5)

where temporal mean is denoted by overbar and fluctuating part is denoted by prime. Since the temporal average of the fluctuating part is zero, equation (5) reduces to

$$\overline{H} = W\rho C_P \int_D^\eta (\overline{U}(\overline{T - T_F}) + \overline{U'T'})\,\mathrm{d}\xi = \overline{\overline{H}} + \tilde{H}$$ (6)

where $\overline{\overline{H}}$ is the contribution from the average velocity and temperature, and $\tilde{H}$ is the contribution from the temporal variability about the mean. Extended Data Table 1 shows the two contributions—the heat flux in all three moorings is caused primarily by the mean, and the contribution from the fluctuations is between 6% and 20%.

Theory

In geostrophic flow[20], the momentum equations are dominated by the Coriolis and the pressure-gradient terms, that is,

$$v = \frac{1}{f\rho}\frac{\partial p}{\partial x}$$ (7)

$$u = -\frac{1}{f\rho}\frac{\partial p}{\partial y}$$ (8)

where (u, v) are the velocity components in the (x, y) directions, f (in s⁻¹) is the Coriolis parameter and p is the hydrostatic pressure. Assuming that the Coriolis parameter is constant and using the Boussinesq approximation[22], it follows from equations (7) and (8) that geostrophic velocity is non-divergent, that is:

$$\frac{\partial u}{\partial x} + \frac{\partial v}{\partial y} = 0$$ (9)

For the simplified case of one active layer, that is, a well mixed layer extending from the bottom to either the surface or to the interface separating an active dense layer from an inactive lighter water mass above it, vertical integration of the continuity equation gives[20–22] (using equation (9) and the fact that the velocities are vertically homogeneous)

$$\frac{\partial \eta}{\partial t} + u\frac{\partial \eta}{\partial x} + v\frac{\partial \eta}{\partial y} - u\frac{\partial D}{\partial x} - v\frac{\partial D}{\partial y} = 0$$ (10)

where η is the upper surface (either the water surface or the dense interface) and D is the bottom elevation. Equation (10) can also be expressed in terms of the layer thickness $H(x, y, t) = \eta(x, y, t) - D(x, y)$ according to:

$$\frac{\partial H}{\partial t} + u\frac{\partial H}{\partial x} + v\frac{\partial H}{\partial y} = 0$$ (11)

Steady solutions to equation (11) have streamlines parallel to lines of constant water column thickness (H), irrespective of the bottom elevation $D(x, y)$ and the pressure (as long as the flow is geostrophic). Equation (11) might appear trivial but the combination of geostrophy and solid upper and lower boundaries has important consequences for the currents entering ice shelf cavities in Antarctica. When an ice shelf is protruding from above, the along-trough flow experienced outside the cavity will be deflected to flow along the ice front instead. Barotropic flow towards Antarctica's ice shelves is thus expected to be blocked from reaching the inner parts of the ice shelf cavities (as seen in Fig. 1). Baroclinic flow, on the other hand, is expected to follow the depth contours into the inner ice shelf cavity.

Laboratory experiments

The laboratory experiments were conducted on the 13-m-diameter rotating platform at Laboratoire des Écoulements Géophysiques et Industriels (LEGI) in Grenoble, France.

A V-shaped channel of size 5 m × 1 m × 0.5 m and a 2% slope (Extended Data Fig. 7) was built at the centre of the turntable (orange dot in Extended Data Fig. 7). Focusing on the dynamics of the flow and ignoring thermodynamic changes such as melting and freezing of ice, a cuboid plexiglass ice shelf with adjustable elevation and tilt was placed at the lower (closed) end of the channel. The tank was filled with 90 cm of fresh water and rotated clockwise (Southern Hemisphere) with a rotation period of 30 s, giving a Coriolis parameter $f = 0.42$ s⁻¹. A source, placed in the centre of the left-hand flank of the channel (looking towards the ice shelf) and resting on the topography, pumped water at 60 l min⁻¹ into the channel. The source was 0.15 m high, 0.25 m wide, 0.25 m long and sloped at the bottom to fit the topography (Extended Data Fig. 7). The outflow area was 0.47 m² and had a honeycomb of small tubes to produce a homogeneous laminar flow. For the barotropic experiments the source water was fresh like the ambient water, and for the baroclinic experiments it was saline and 2 kg m⁻³ denser than the ambient water. Drainage and a skimmer kept the water level constant.

Neutrally buoyant particles (60 μm Dantec Dynamics particles) in the source water were illuminated by a horizontal laser plane (Extended Data Fig. 8) in order to visualize the flow. Two cameras with pixel resolution 2,560 × 2,160 pixels were mounted above the channel. The footprint of both cameras (Extended Data Fig. 7) gave a resolution of 0.6 mm per pixel. The laser shifted through depth levels starting near the bottom of the channel. For the barotropic experiments, 12 different depth levels were used with a vertical distance of dz = 6.2 cm. In order to resolve better the faster-moving dense current and focus on the lower part of the channel, seven different depth levels with dz = 5.8 cm were used in

Article

the baroclinic experiments. At each level, 30 (barotropic experiments) or 20 (baroclinic experiments) consecutive images were taken by both cameras with 0.1 s intervals giving a total of 60 s for a complete cycle through all depth levels. The obtained images were used for particle image velocimetry (PIV) calculations with UVMAT software developed at LEGI (for details see http://servforge.legi.grenoble-inp.fr/projects/soft-uvmat). Independent results were also obtained with another software package, MatPIV (https://www.mn.uio.no/math/english/people/aca/jks/matpiv), and found to agree with UVMAT. Using the pixel per image value, that is, 0.6 mm/0.5 s for barotropic experiments (every five images were used) and 0.6 mm/0.1 s for baroclinic experiments, the velocity error was 1.2 mm s^{-1} for the barotropic and 6 mm s^{-1} for the baroclinic experiments. The obtained 25 (or 19 for baroclinic experiments) velocity fields for each level were then averaged, which lowered the error further. Figure 4 shows the average of 4–5 cycles at one level, starting at the time when the leading edge reached the ice front, together with the temporal standard deviation of the velocity for that level (cyan bars) and the error (magenta bars). Outliers (defined as velocities for which the standard deviation exceeds 10 times the average standard deviation) were identified and filtered out. The vertical sections (Fig. 4d–f) were created from the parts of the horizontal slices that occupied ±2 cm around the green and magenta lines in Fig. 4.

In addition to the top-view cameras, a side-view camera was mounted outside a glass wall at the side of the tank and GoPro cameras were lowered into the water to get side-view images (Fig. 3 and Extended Data Fig. 8). In the side-view images, fluorescent dye (rhodamine) was used for visualization.

The topography was built to mimic a submarine trough topography with depth variations of same magnitude as the ice shelf draught, in similarity with the observations. Geostrophic balance was ensured by choosing flow rates and rotation rates so that both the Ekman number Ek (that is, the frictional force compared to the Coriolis force[20]) and the Rossby number[20] (that is, the inertial forces compared to the Coriolis force) were smaller than one. The values of the various scales and the non-dimensional numbers are shown in Extended Data Table 2. While the Ekman number was clearly negligible (0.002–0.004), the Rossby number was 0.14–0.2, meaning that ageostrophic effects may amend the process, particularly in regions where the velocity might be larger.

Before each experiment, the platform was spun up for 2–3 h to reach solid body rotation, which was determined by observing the movement of particles. Each experiment was started by opening the source. After about 5–10 min (faster for baroclinic flow), a current moving towards the ice shelf developed over the sloping part of the topography (Extended Data Fig. 8). Behind the leading edge of the current, a semi-steady flow with regions of slower and faster flow moving in the direction of the ice shelf developed (Extended Data Fig. 8d). After interaction with the ice shelf (15–30 min after experiment start), a counter-current on the opposite side developed, after which the experiment ended.

The baroclinic flow developed faster, was more steady, and was not influenced by the presence of the ice shelf. Instead of returning on the opposite side, the baroclinic flow slowly filled the ice shelf cavity with dense water (Extended Data Fig. 8). More details from the experiments, including detailed drawings and diary, are provided at http://servforge.legi.grenoble-inp.fr/projects/pj-coriolis-17iceshelf.

Data availability

The mooring data analysed during the current study (raw data for Figs. 1, 2 and Extended Data Figs. 1–6) are available at the Norwegian Marine Data Centre (https://doi.org/10.21335/NMDC-1721053841, GW1, 2)[40] and at the SOOS database at NODC (https://doi.org/10.25921/n07g-f935 and https://doi.org/10.25921/6pwp-1791, GW3). Raw data obtained from the PIV calculations (raw data for Fig. 4 and Extended Data Fig. 9) are available at Zenodo (https://zenodo.org/record/3543624).

Code availability

The PIV calculations were conducted with the matlab software UVMAT developed at LEGI available at http://servforge.legi.grenoble-inp.fr/projects/soft-uvmat. Independent results were also obtained with the MatPIV package available at https://www.mn.uio.no/math/english/people/aca/jks/matpiv.

36. Taylor, J. A. & Jonas, A. M. Maximising data return: towards a quality control strategy for managing and processing TRDI ADCP data sets from moored instrumentation. In *2008 IEEE/OES 9th Working Conference on Current Measurement Technology* 80–88 (IEEE, 2008); available at https://doi.org/10.1109/CCM.2008.4480848 (2008).
37. IOC, SCOR & IAPSO. *The International Thermodynamic Equation of Seawater, 2010: Calculation and Use of Thermodynamic Properties.* IOC Manuals and Guides No. 56 (UNESCO, 2010).
38. Wesche, C., Jansen, D. & Dierking, W. Calving fronts of Antarctica: mapping and classification. *Remote Sens.* **5**, 6305–6322 (2013).
39. Fofonoff, N. P. & Millard, R. C. *Algorithms for Computation of Fundamental Properties of Seawater.* UNESCO Technical Papers in Marine Science 44 (UNESCO, 1983).
40. Darelius, E., Fer, I., Assmann, K. & Kim, T. W. Physical oceanography from Mooring UiB1 and UiB4 in the Amundsen Sea. https://doi.org/10.21335/NMDC-1721053841 (University of Bergen, 2018).

Author contributions A.K.W. proposed the research. A.K.W., N.S., E.D. and K.M.A. wrote the first draft. J.S. assisted with analyses and a repository of laboratory data. All authors contributed to the laboratory experiments, to data processing, and/or to the field work. A.K.W., N.S., S.V. and A.K.M. prepared the figures. All authors read and commented on the text.
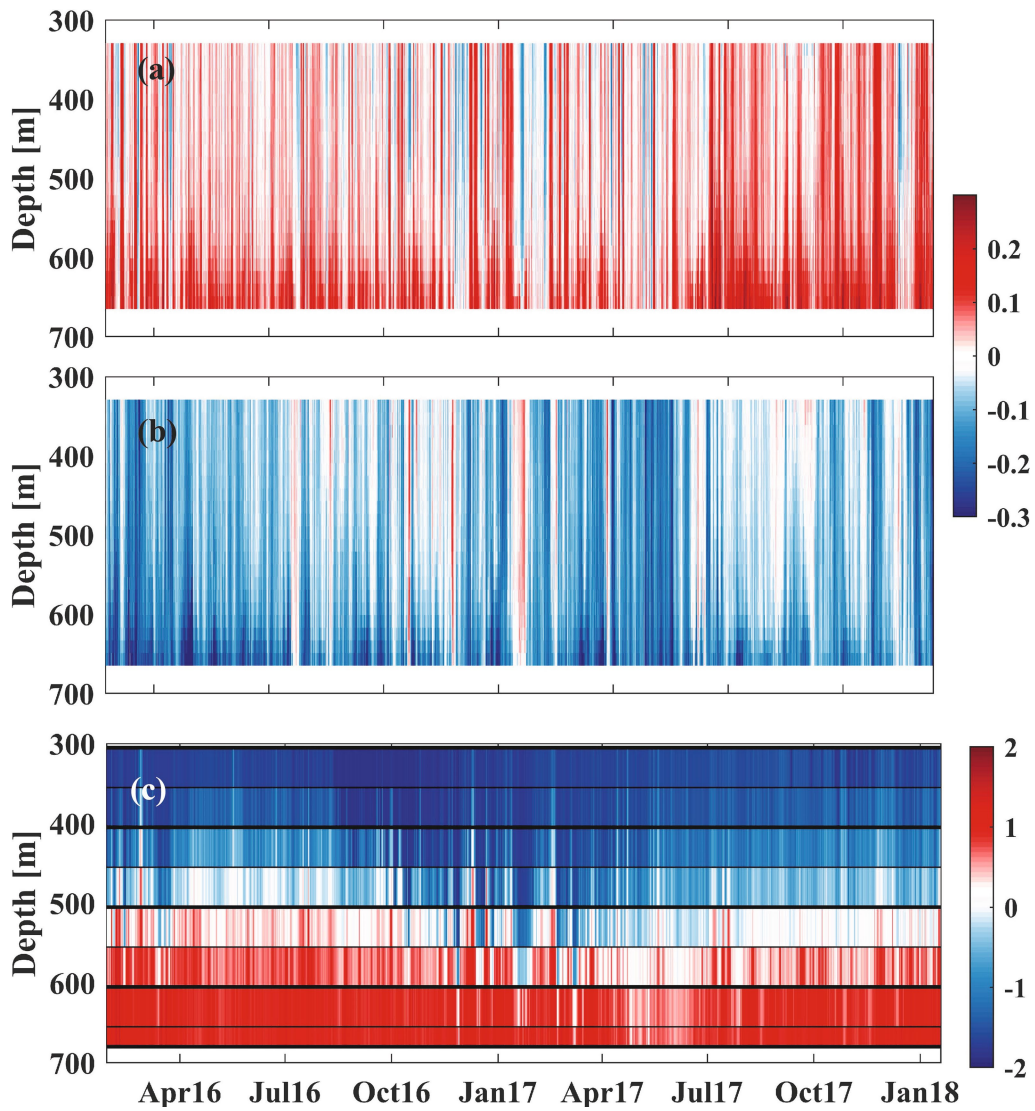
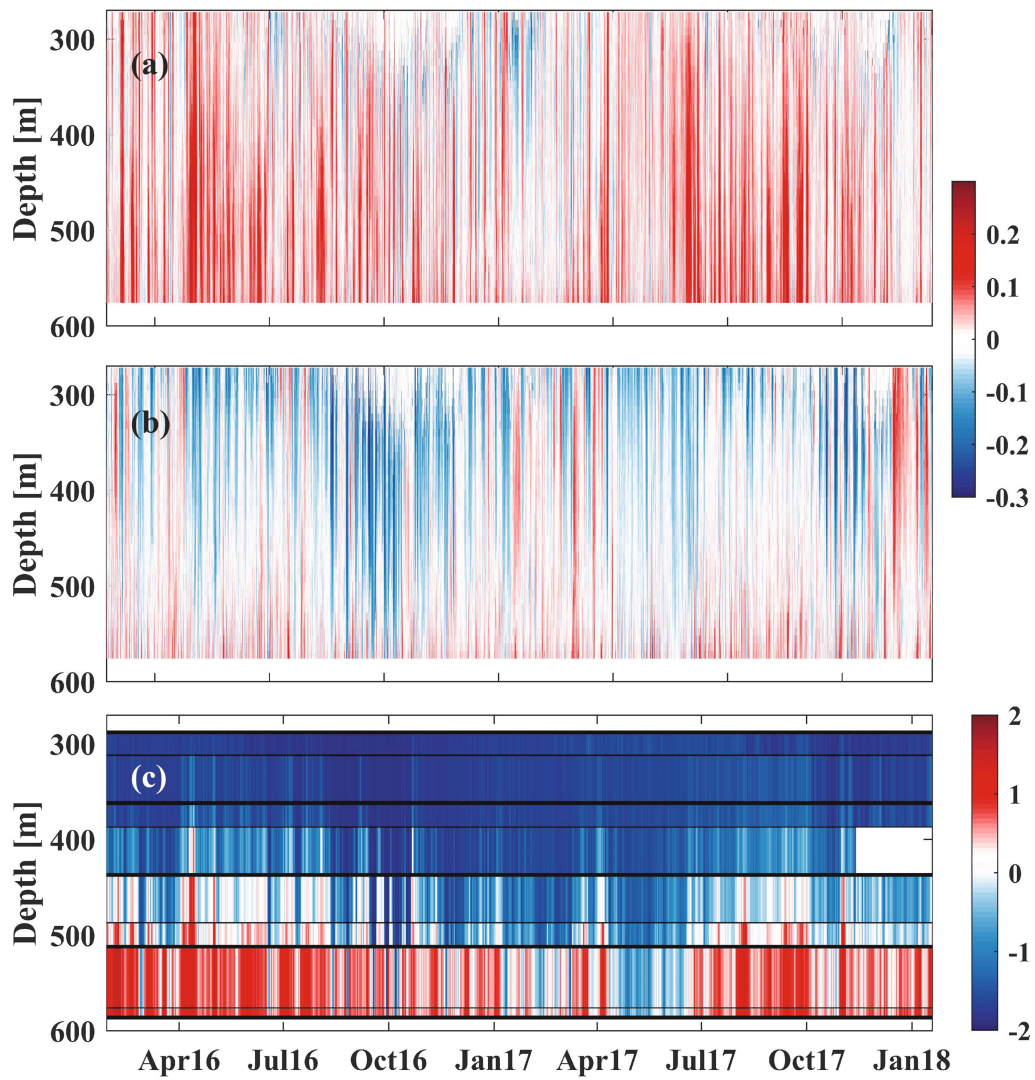**Extended Data Fig. 1 | Two year time series of velocity and temperature from the GW1 mooring. a–c**, Time series of eastward velocity (**a**; in m s⁻¹), northward velocity (**b**; in m s⁻¹) and temperature (**c**; in °C) for the GW1 mooring. Black lines in **c** indicate positions of Microcats (instruments that measure temperature and salinity; thick lines) and SBE56 (instruments that measure temperature; thin lines).
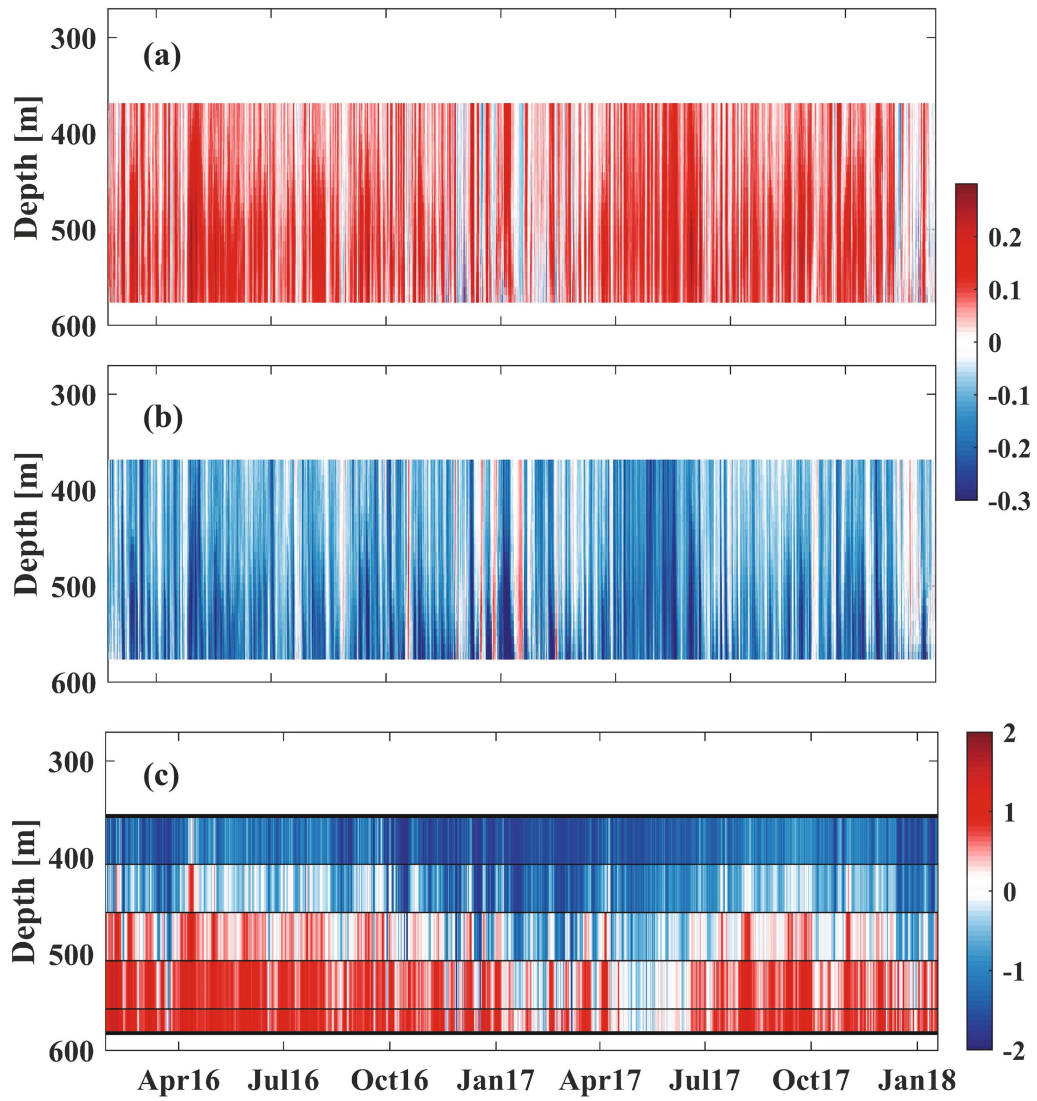
Extended Data Fig. 2 | Two year time series of velocity and temperature from the GW2 mooring. a–c, Time series of eastward velocity (**a**; in m s⁻¹), northward velocity (**b**; in m s⁻¹) and temperature (**c**; in °C) for the GW2 mooring. Black lines in **c** indicate positions of Microcats (thick lines) and SBE56 (thin lines).

Extended Data Fig. 3 | Two year time series of velocity and temperature from the GW3 mooring. a–c, Time series of eastward velocity (**a**; in m s⁻¹), northward velocity (**b**; in m s⁻¹) and temperature (**c**; in °C) for the GW3 mooring. Black lines in **c** indicate positions of Microcats (thick lines) and SBE56 (thin lines).
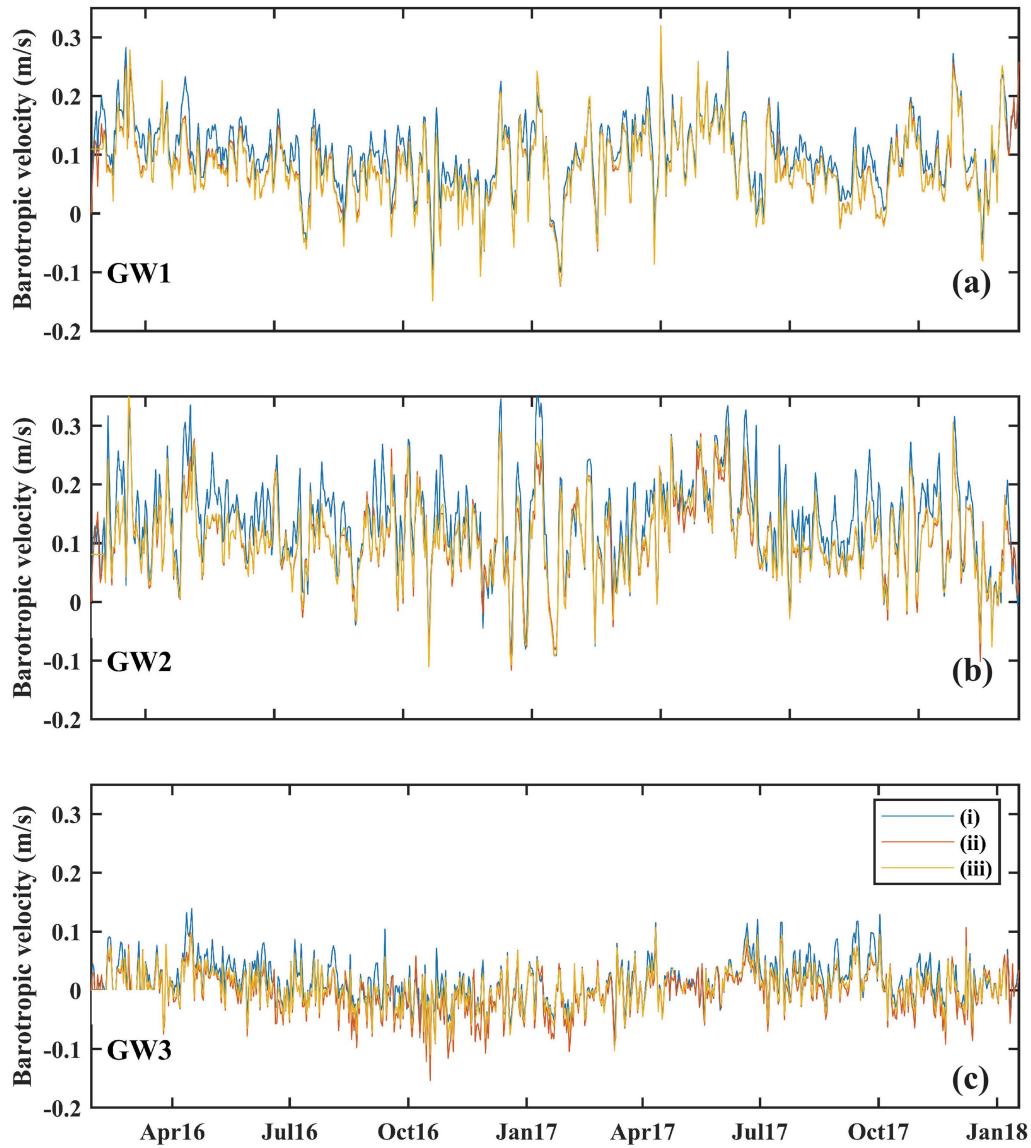
Extended Data Fig. 4 | Comparison of methods for calculating the barotropic current component. a–**c**, Each panel shows the along-slope barotropic current component calculated in three ways (see Methods): blue curve, option (i), using the vertical average; red curve, option (ii), using the vertical average of the water more than 150 m above the seabed; and orange curve, option (iii), using the vertical average of water above the −0.5 °C isotherm. Three-day-averaged results are shown for mooring GW1 (**a**), mooring GW2 (**b**) and mooring GW3 (**c**).
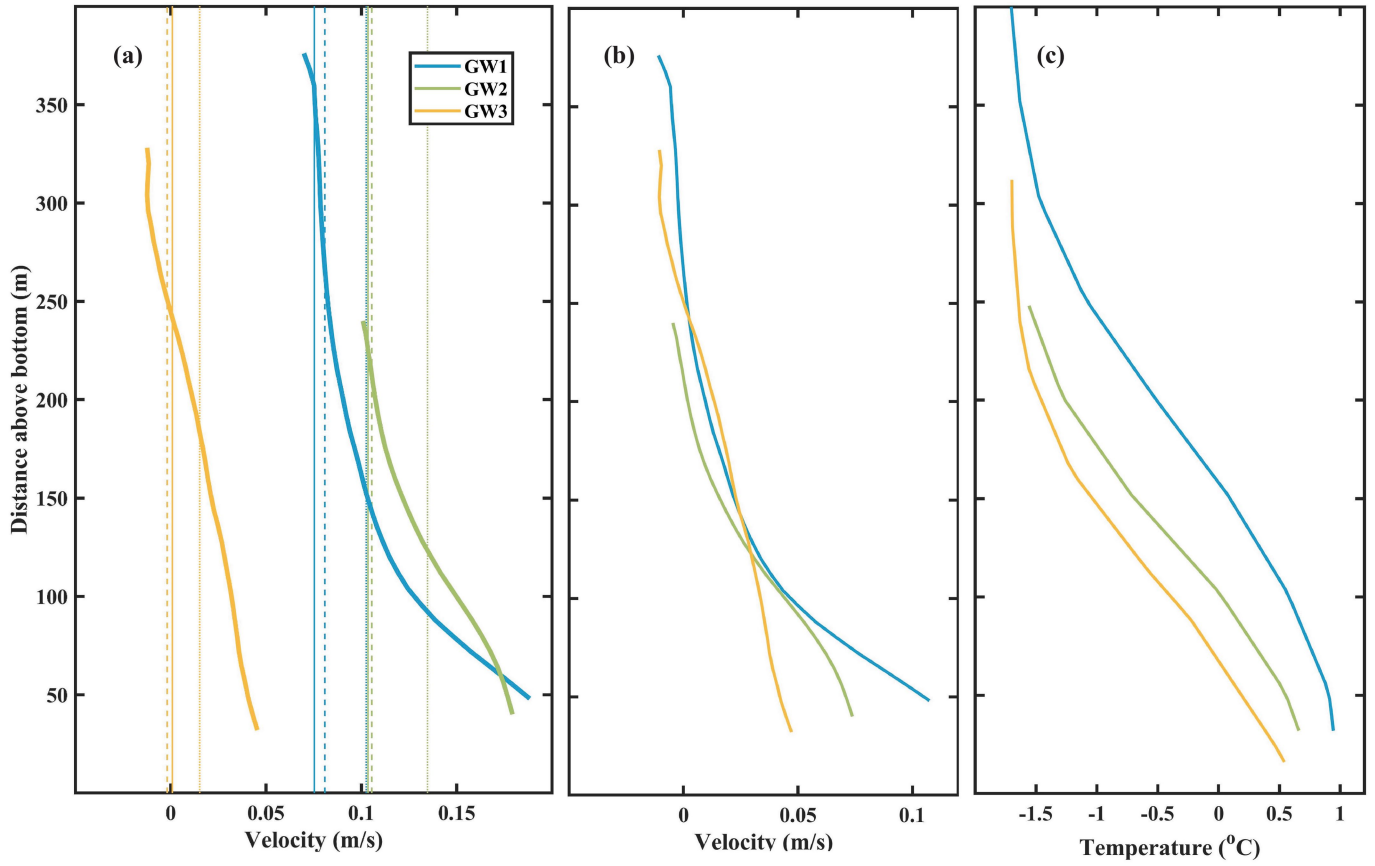
Extended Data Fig. 5 | The barotropic velocity is larger for GW1 and GW2 than GW3, the baroclinic velocity and the temperature increase towards the bottom. a, Thick lines show average along-slope velocities as a function of distance above bottom, with colours indicating mooring (see key). Thin vertical lines show the barotropic components estimated according to method (i) (dotted lines), method (ii) (dashed lines), and method (iii) (solid lines). **b**, Baroclinic velocity components as a function of distance above bottom. **c**, Average temperature as a function of distance above bottom.
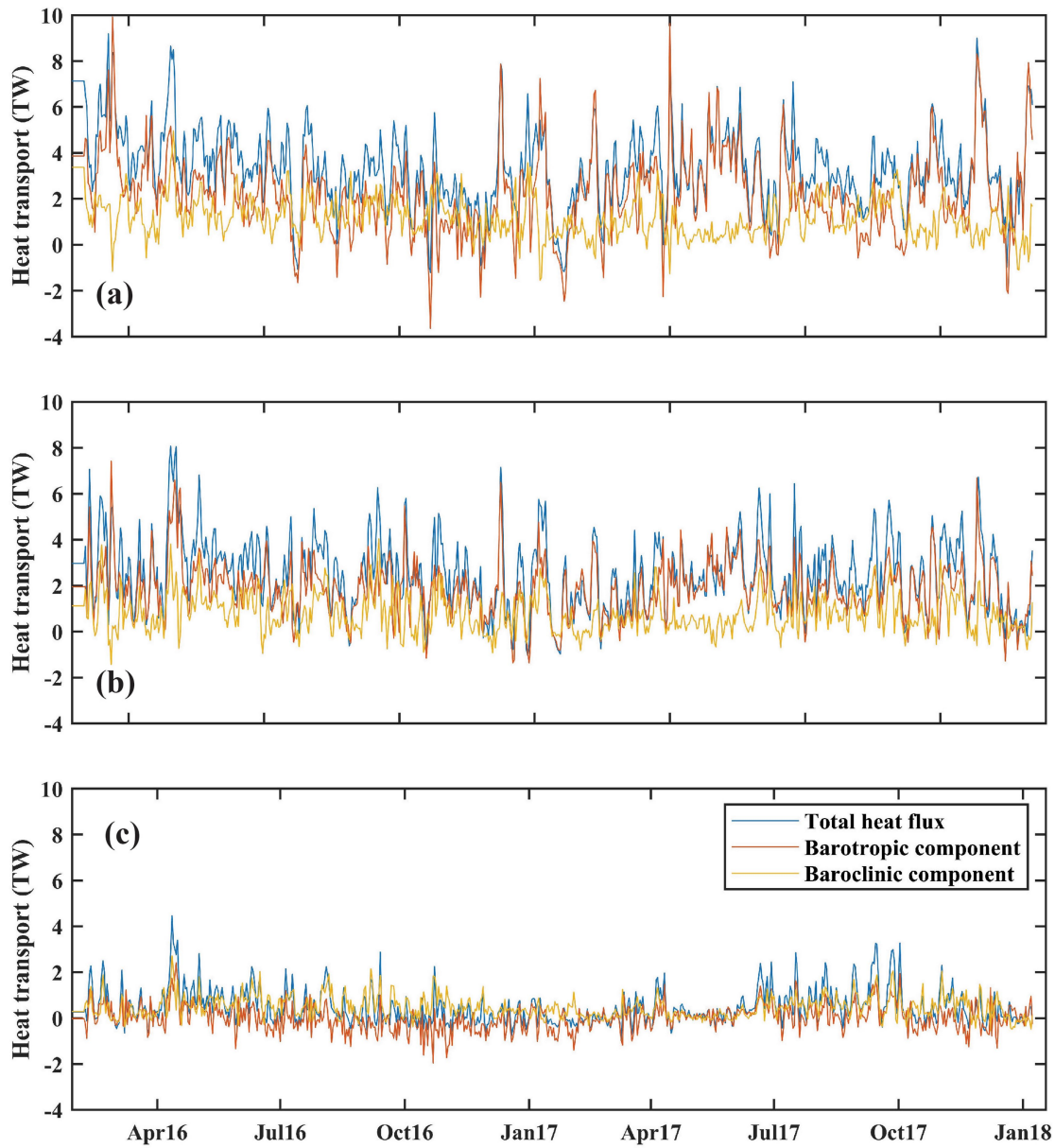
Extended Data Fig. 6 | The barotropic heat flux component is larger than the baroclinic component for GW1 and GW2. a–c, Each panel shows the time series of total heat flux (blue curve) and the barotropic and baroclinic components (respectively, red and orange curves) using equation (2) and definition (ii) of barotropic velocity, as described in Methods. **a**, Mooring GW1; **b**, mooring GW2; and **c**, mooring GW3.
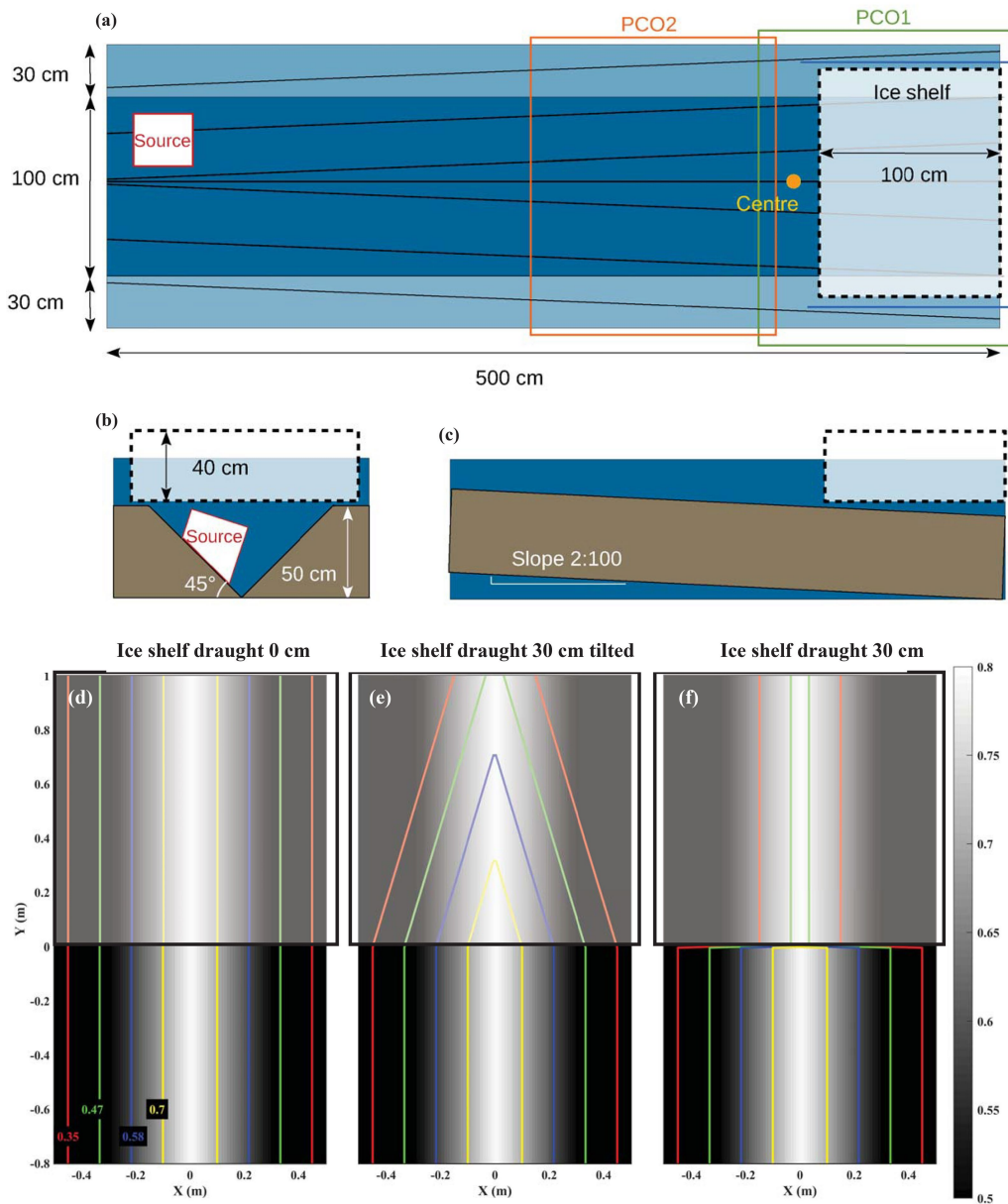
Extended Data Fig. 7 | Experiment set-up and dimensions. a, Top view drawing of V-shaped channel (blue), ice shelf (white), camera views (PCO1, green; PCO2, orange) and the source (to scale). **b**, Side view drawing looking into the ice shelf facing south (right side in **a**). **c**, Side view drawing looking east (top of **a**). **d**–**f**, Top views of topography (grey scale bar indicates depth (in metres)) and water column thickness (coloured lines, labels, in metres) for ice shelf draughts of 0 cm (**d**), 30 cm, tilted (**e**), and 30 cm, horizontal (**f**).
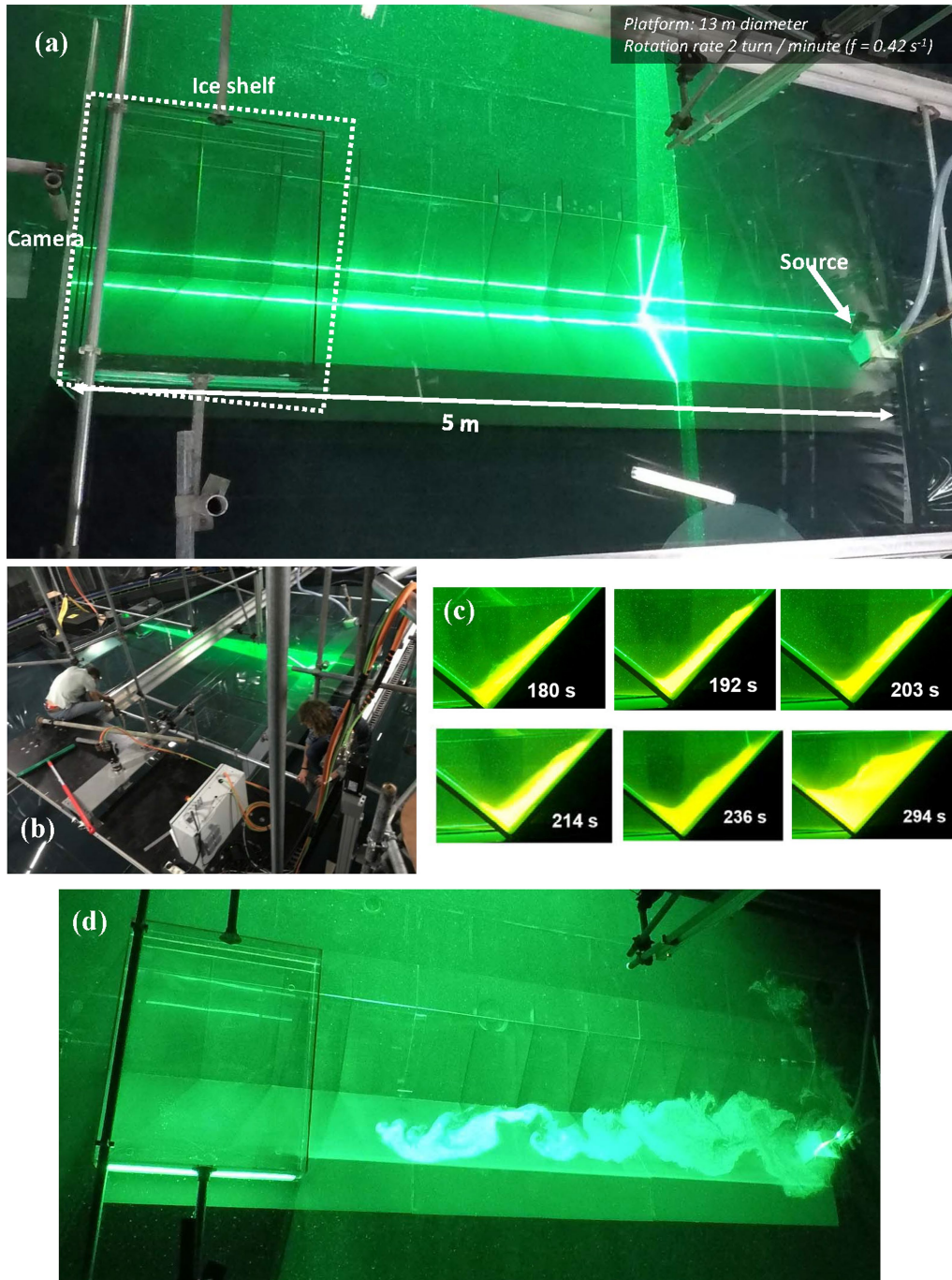
Extended Data Fig. 8 | Photographs of the experiments. a, Top view showing the experimental set-up with the horizontal and vertical laser sheets. **b**, Technicians and students preparing for an experiment. **c**, Time series showing the ice shelf cavity filling up with dense water for the baroclinic experiments. **d**, Top view photograph showing a barotropic current moving towards the ice shelf. See Methods for details.
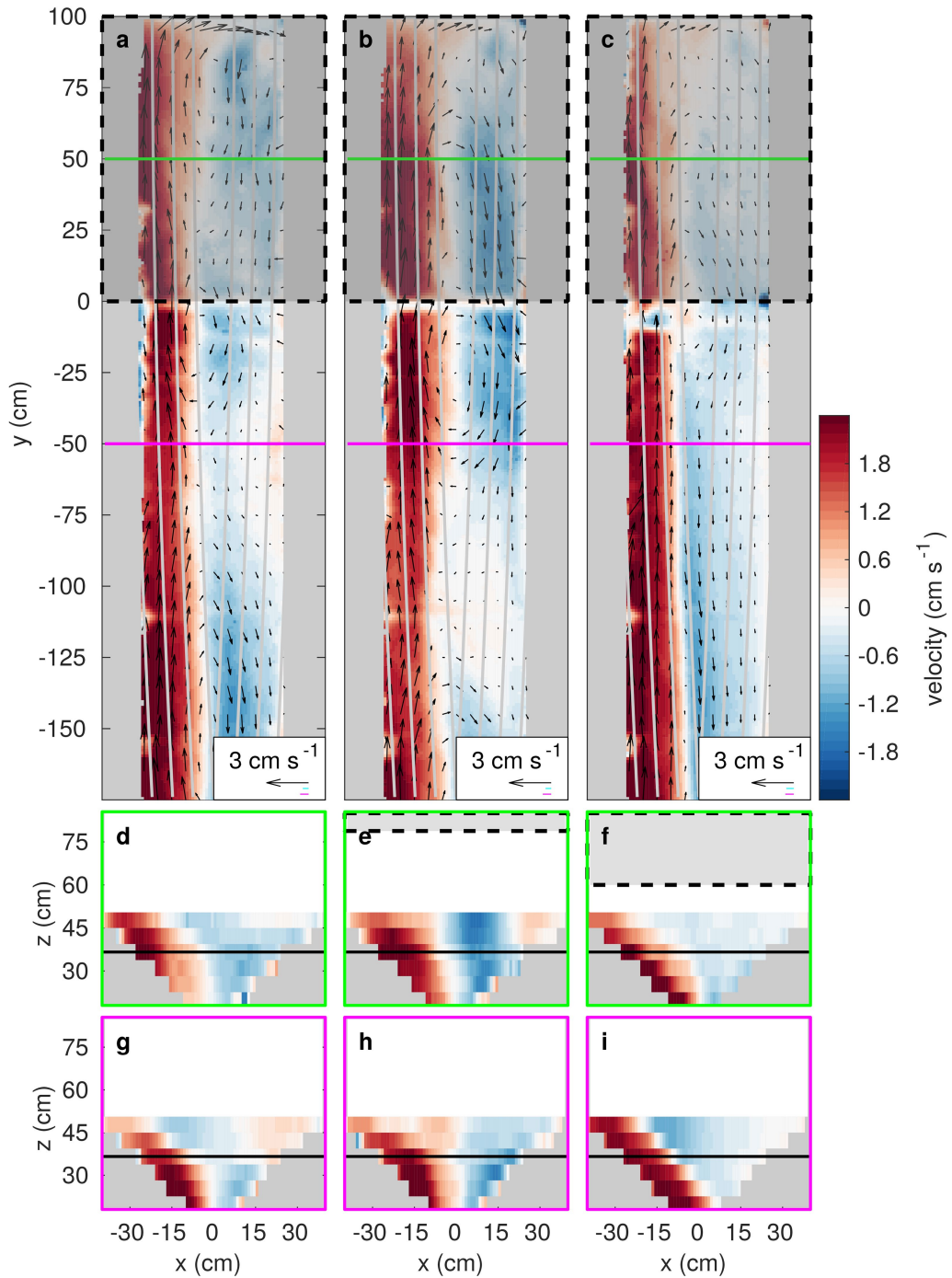
Extended Data Fig. 9 | No blocking of depth-varying currents in laboratory.
a–i, Horizontal velocities from the laboratory experiments for baroclinic flow
with the three different ice shelf configurations (Fig. 3b–d). Colours indicate
velocity in the *y* direction, arrows indicate velocity vectors. **a–c**, Velocities at
the horizontal plane in the centre of the current (black lines in **d–i**). **d–f**,
Velocities at vertical sections underneath the ice shelf (green lines in **a–c**) and

g–i in front of it (magenta lines in **a–c**). Dashed and shadowed rectangles
indicate the ice shelf, grey shading indicates topography and grey lines are
bathymetric lines that the current is expected to follow. White areas are not-
measured or missing data. The cyan bar beneath the scale arrow in **a–c** indicate
the temporal standard deviation of the velocity, and the magenta bar indicates
the error (Methods).

Extended Data Table 1 | Barotropic heat transport component is large compared to baroclinic

	GW1	GW2	GW3
H	2.8 TW	2.27 TW	0.47 TW
$\overline{\overline{H}}$	2.64 TW (94%)	2.14 TW (94%)	0.38 TW (80%)
$\tilde{H}$	0.16 TW (6%)	0.13 TW (6%)	0.09 TW (20%)
H_{BT} (method (i))	2.49 TW (89%)	2.11 TW (93%)	0.28 TW (60%)
H_{BC} (method (i))	0.31 TW (11%)	0.16 TW (7%)	0.19 TW (40%)
H_{BT} (method (ii))	1.96 TW (70%)	1.61 TW (71%)	0.01 TW (3%)
H_{BC} (method (ii))	0.84 TW (30%)	0.66 TW (29%)	0.46 TW (97%)
H_{BT} (method (iii))	1.88 TW (67%)	1.59 TW (70%)	0.05 TW (10%)
H_{BC} (method (iii))	0.92 TW (33%)	0.68 TW (30%)	0.42 TW (90%)

Average heat flux (H) and its barotropic (equation (4)) and baroclinic (equation (3)) components using different definitions of barotropic velocity: method (i), vertical average over the entire measured water column; method (ii), vertical average over the measured water column more than 150 m above the bottom; and method (iii), vertical average over the measured water column above the −0.5 °C isotherm (see Methods). Also shown is the part of the heat flux induced by the average velocity and temperature ($\overline{H}$) and their fluctuating components ($\tilde{H}$) according to equation (6).

Extended Data Table 2 | Non-dimensional scales are similar in laboratory experiments and observations

Symbol [unit]	Laboratory	Obervations	Description
U [m s^{-1}]	0.03	0.2	Velocity
$\Delta\rho$ [kg m^{-3}]	2	0.3	Density difference
f [s^{-1}]	0.42	10^{-4}	Coriolis parameter
H [m]	0.5	500	Depth
L [m]	0.5	10^4	Width
ν [m^2 s^{-1}]	10^{-6}	10^{-4}	Viscosity
$\delta_E = \sqrt{\nu/f}$ [m]	0.0015	1	Ekman depth
$Ek = \delta_E^2/H^2$	$0.9 \cdot 10^{-5}$	$0.4 \cdot 10^{-5}$	Ekman number
$L_R = U/f$ [m]	0.07	2000	Rossby radius
$Ro = L_R/L$	0.14	0.2	Rossby number

Scale values for velocity (U), density difference ($\Delta\rho$), Coriolis parameter (f), depth (H), width (L), molecular (in laboratory) or turbulent (in field) viscosity (ν) and the derived Ekman depth (δ_E), Ekman number (Ek), Rossby radius (L_R) and Rossby number (Ro). Observational parameters for velocity and density difference were obtained from the GW1 and GW2 mooring data, while the bathymetric parameters were obtained from ref. [31]. The viscosity scale is a bulk eddy viscosity[22].